ISSN: 1554-8627 (Print) 1554-8635 (Online) Journal homepage: www.tandfonline.com/journals/kaup20

ATG16L1 WD domain and linker regulates lipid trafficking to maintain plasma membrane integrity to limit influenza virus infection

Benjamin Bone, Luke Griffith, Matthew Jefferson, Yohei Yamauchi, Thomas Wileman & Penny P. Powell

To cite this article: Benjamin Bone, Luke Griffith, Matthew Jefferson, Yohei Yamauchi, Thomas Wileman & Penny P. Powell (2025) ATG16L1 WD domain and linker regulates lipid trafficking to maintain plasma membrane integrity to limit influenza virus infection, *Autophagy*, 21:9, 1911-1926, DOI: [10.1080/15548627.2025.2482516](https://doi.org/10.1080/15548627.2025.2482516)

To link to this article: <https://doi.org/10.1080/15548627.2025.2482516>



© 2025 The Author(s). Published by Informa UK Limited, trading as Taylor & Francis Group.



View supplementary material [↗](#)



Published online: 03 Apr 2025.



Submit your article to this journal [↗](#)



Article views: 1932



View related articles [↗](#)



View Crossmark data [↗](#)

RESEARCH PAPER



ATG16L1 WD domain and linker regulates lipid trafficking to maintain plasma membrane integrity to limit influenza virus infection

Benjamin Bone^{a*}, Luke Griffith^{a*}, Matthew Jefferson^a, Yohei Yamauchi^{b,c}, Thomas Wileman^a, and Penny P. Powell^{ib a}

^aBiomedical Research Centre, Norwich Medical School, University of East Anglia, Norwich, Norfolk, UK; ^bMolecular Medicine Laboratory, Institute of Pharmaceutical Sciences, D-CHAB, ETH Zurich, Zurich, Switzerland; ^cDepartment of Virology, Graduate School of Medicine, Nagoya University, Japan

ABSTRACT

The non-canonical functions of autophagy protein ATG16L1 are dependent on a C-terminal WD domain. Recent studies show that the WD domain is required for conjugation of LC3 to single membranes during endocytosis and phagocytosis, where it is thought to promote fusion with lysosomes. Studies in cells lacking the WD domain suggest additional roles in the regulation of cytokine receptor recycling and plasma membrane repair. The WD domain also protects mice against lethal influenza virus *in vivo*. Here, analysis of mice lacking the WD domain (Δ WD) shows enrichment of cholesterol in brain tissue suggesting a role for the WD domain in cholesterol transport. Brain tissue and cells from Δ WD mice showed reduced cholesterol and phosphatidylserine (PS) in the plasma membrane. Cells from Δ WD mice also showed an intracellular accumulation of cholesterol predominantly in late endosomes. Infection studies using IAV suggest that the loss of cholesterol and PS from the plasma membrane in cells from Δ WD mice results in increased endocytosis and nuclear delivery of IAV, as well as increased *Ifnb*/*Ifn β* and *Isg15* gene expression. Upregulation of *Il6*, *Ifnb* and *Isg15* mRNA were observed in “*ex vivo*” precision cut lung slices from Δ WD mice both at rest and in response to IAV infection. Overall, we present evidence that regulation of lipid transport by the WD domain of ATG16L1 may have downstream implications in attenuating viral infection and limiting lethal cytokine signaling.

ARTICLE HISTORY

Received 28 August 2024
Revised 12 March 2025
Accepted 18 March 2025

KEYWORDS

ATG16L1 WD domain;
cholesterol; cytokine storm;
influenza virus; interferon;
non-canonical autophagy



Abbreviations: BMDM: bone marrow-derived macrophages, CASM: conjugation of ATG8 to single membranes, CCD: coil-coil domain, IAV: influenza virus A, IFIT1: interferon-induced protein with tetratricopeptide repeats 1, IFITM3: interferon induced transmembrane protein 3, IFN: interferon, ISG15: ISG15 ubiquitin-like modifier, LANDO: LC3-associated endocytosis, LAP: LC3-associated phagocytosis, LDL: low density lipoprotein, NP: nucleoprotein, PS: phosphatidylserine, WD: WD40-repeat-containing C-terminal domain, WT: wild type.

Introduction


ATG16L1 plays an important role within the ATG12–ATG5–ATG16L1 complex during autophagy where it facilitates conjugation of ATG8 mammalian orthologs such as LC3 onto double-membraned phagophores [1]. ATG16L1 also functions within non-canonical pathways during conjugation of LC3 to single-membraned compartments, such as phagosomes during LC3-associated phagocytosis (LAP) and to endo-lysosome membranes during conjugation of ATG8 to single membranes (CASM) and LC3-associated endocytosis (LANDO) [2–4]. Structural and functional analysis of ATG16L1 has identified distinct domains that contribute to these different functions. The N terminus contains an ATG5-binding domain and coiled-coil domain (CCD) required for autophagy where a WIPI binding site anchors ATG16L1 to sites of phagophore expansion [5,6,7]. The C-terminal WD40 domain containing seven WD repeats is not required for autophagy but is required for the conjugation of

LC3 onto single membranes through during CASM [8–10]. In the best characterized example of CASM an increased pH in endo-lysosome compartments activates the assembly of the vacuolar-type H⁺-translocating ATPase (V-ATPase) where it provides a binding site for the WD domain of ATG16L1 and subsequent recruitment of ATG12–ATG5 and conjugation of LC3 [11, 12, 13]. This has been called the V-ATPase-ATG16L1 axis and it can be disrupted by a *Salmonella* effector protein called SopF to promote replication [14–16].

ATG16L1 also contains an extended, unstable linker region between the CCD and WD repeats and expression of a T300A variant in the linker is associated with increased risk of Crohn disease and abnormalities in Paneth cell lysozyme distribution and in goblet cell morphology [17]. In a previous study [9] we truncated ATG16L1 after the N-terminal CCD by introducing two stop codons into exon 6 immediately after glutamate E230 required for WIPI2

CONTACT Penny P. Powell  P.Powell@uea.ac.uk  Biomedical Research Centre, Norwich Medical School, University of East Anglia, Earlham Road, Norwich, Norfolk NR4 7TJ, UK

*These authors contributed equally to this work.

 Supplemental data for this article can be accessed online at <https://doi.org/10.1080/15548627.2025.2482516>

© 2025 The Author(s). Published by Informa UK Limited, trading as Taylor & Francis Group.

This is an Open Access article distributed under the terms of the Creative Commons Attribution License (<http://creativecommons.org/licenses/by/4.0/>), which permits unrestricted use, distribution, and reproduction in any medium, provided the original work is properly cited. The terms on which this article has been published allow the posting of the Accepted Manuscript in a repository by the author(s) or with their consent.

binding [14]. For simplicity we call these Δ WD mice but it should be appreciated that they lack both the linker and the WD repeat domain. Autophagy assays such as LC3 puncta and LC3-II formation and SQSTM1/p62 degradation in MEFs, skin fibroblasts and bone marrow-derived macrophages from the mice show that canonical autophagy is unaffected by the mutation [9,18,19]. Size exclusion chromatography of liver lysates showed that the truncated ATG16L1 (1–230) forms a high molecular weight complex containing ATG12–ATG5 and WIPI2 “*in vivo*”. Furthermore, the liver, kidney, brain and muscle of these mice maintain levels of autophagy cargoes such as LC3 and SQSTM1 similar to littermate controls, and do not show accumulation of SQSTM1/p62 in inclusions and tissue damage associated with loss of autophagy “*in vivo*”. Taken together the data show that autophagy powered by the ATG16L1 lacking both the WD and linker domains is sufficient for maintaining canonical autophagy and tissue homeostasis “*in vivo*”.

In contrast, bone marrow-derived macrophages from Δ WD mice show defects in LAP and antigen presentation [9,18,19]. Studies using Δ WD mice also show that the WD domain regulates cytokine receptor trafficking during IL10 signaling [20] and is required for recycling beta-amyloid receptors in primary microglia which is essential for maintaining cognitive health, with mice lacking the WD domain developing spontaneous Alzheimer disease (AD) [21]. We have also shown that the WD domain also plays an important role in protecting mice from influenza virus A (IAV) infection [18]. The Δ WD mice are highly susceptible to IAV infection, with increased weight loss, virus lung titer, and mortality following IAV infection when compared to WT littermate controls and increased virus replication in the airways leads to a cytokine storm, pneumonia and increased mortality, thus raising the possibility of a yet undescribed role for this domain that may directly or indirectly provide antiviral protection. While decreased degradation by the LAP, CASM and LANDO pathways due to dysfunctional conjugation machinery may explain the heightened susceptibility, at present direct evidence of the WD domain and linker region in virus degradation is lacking. Cell culture experiments have shown that this region slows endocytosis of IAV and fusion of IAV envelope with endosomes resulting in slower delivery of IAV genomes into cells and delayed cytokine signaling [18]. Biophysical characteristics of membranes, such as stability, are reliant upon the cholesterol concentration, with it being widely understood that the cholesterol concentrations of interacting membranes can influence viral infection [22], including IAV infection [23,24]. An example is the antiviral actions of IFITM3 (interferon induced transmembrane protein 3) which disrupts cholesterol homeostasis to raise endosome cholesterol to slow virus entry [25]. Taken together, in this study we assume that some action the WD domain is involved in cellular cholesterol homeostasis to slow viral entry. Indeed, recent data has demonstrated that ATG16L1 is involved in lysosomal exocytosis, which promotes plasma membrane repair following membrane damage by bacterial pore-forming toxins, and during *Listeria monocytogenes* infection, a function which limits cell to cell spread [26]. Plasma membrane repair involves efflux of cholesterol from

lysosomes to the plasma membrane, a process dependent upon the WD domain of ATG16L1 and the ATG12–ATG5 conjugant, but not reliant upon other proteins crucial for autophagy [27].

Here we build on our previous study [18] and find an unconventional role for the WD domain in protecting mice from IAV infection through control of cholesterol distribution. We performed *ex vivo* infection challenges of precision cut lung slices from WT and Δ WD mice and show increased infection and elevated cytokine expression in Δ WD tissue. Following this, we monitored by fluorescence microscopy and qPCR the early infection events of IAV, observing an enhanced entry of IAV into Δ WD primary mouse embryonic fibroblasts (MEFs). To investigate whether cholesterol has a role in this increased viral entry, we used probes and chemical assays for cholesterol to show that there was an altered intracellular distribution with accumulation in late endosomes in Δ WD cells, and a depletion in the plasma membrane of brain tissue in Δ WD mice. Pharmacological modification of cholesterol distribution restored cholesterol and phosphatidylserine to the plasma membrane and decreased IAV infection in Δ WD cells and tissues. Taken together, we show that the WD domain of ATG16L1 maintains the integrity and lipid composition of the plasma membrane *in vivo*, and we argue that this slows IAV escape from endosomes and attenuates the innate immune response to IAV. This work adds to the number of unconventional activities of the WD domain of ATG16L1.

Results

ATG16L1 WD domain suppressed cytokine production by slowing IAV endocytosis

To build on the findings from our previous study which compared IAV infection of Δ WD and WT mice [18], we extended our work to investigate IAV infection in a precision cut lung slice tissue *ex vivo* model comprising epithelial, mesenchymal and resident immune cell types. Lung slices from WT and Δ WD mice (Figure 1A) were infected with IAV X31 for 2 h before infection media was removed and slices were incubated in media for 24, 48 and 72 h post infection (hpi). Virus secreted into media over 24 to 72 hpi was titrated on MDCK cells by plaque assay (Figure 1B). As previously seen, virus production was higher at all time points in lung slices from Δ WD mice compared to WT controls, this difference reaching statistical significance at 48 and 72 hpi (Figure 1B). Expression of mRNA for cytokines *Isg15*, *Ifitm3* and *Ifit1/Isg56* and the proinflammatory cytokine gene *Il6* was analyzed, with elevated levels observed in Δ WD lung slices compared to WT controls at 16 hpi (Figure 1C), the average relative quantity of *Ifitm3* and *Il6* increased nearly 3–4-fold. The results confirm our previous work and establish that the WD domain of ATG16L1 reduces IAV replication in lung slices *ex vivo* and that this reduces inflammation by reducing interferon signaling and pro-inflammatory cytokine production. In this way the lung slices taken from Δ WD mice recapitulate the cytokine storm induced by IAV in the Δ WD mice *in vivo* [18].

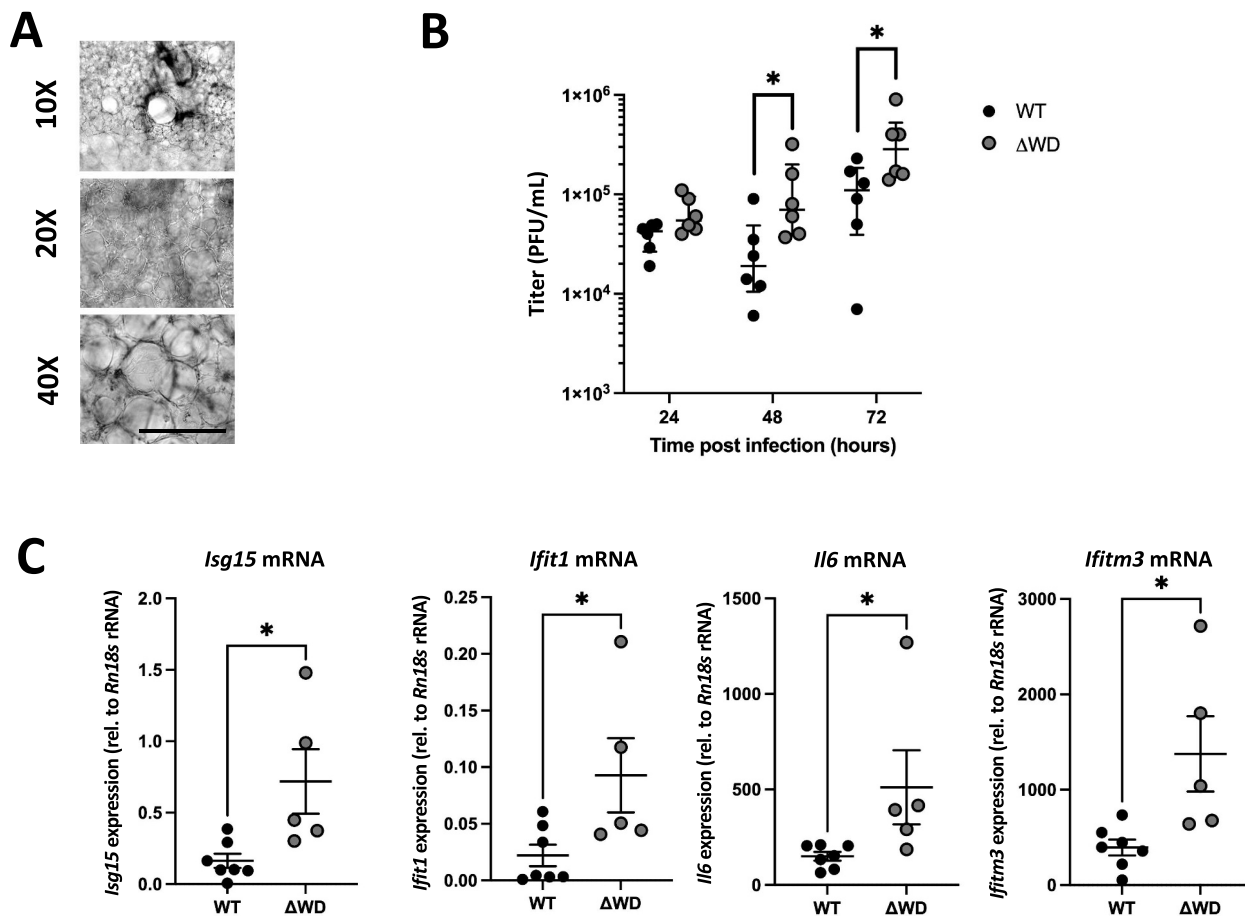


Figure 1. Lung explants from Δ WD mice demonstrated increased IAV replication and cytokine responses. (A) *In vivo* brightfield images of mouse lung explants at 10 \times , 20 \times and 40 \times magnification showing lung architecture of vessels, bronchioles, and cilia. Scale bar: 150 μ m (B) titration of IAV X31 replication in WT and Δ WD independent lung slices from 6 mice, at 24, 48 and 72 hpi, virus was titrated on MDCK cells and PFU/mL (+SEM) shown per slice for the different time points. Mann Whitney U test: $*p < 0.05$. $n = 6$. (C) Relative expression (+SEM) of *Ift1*, *Isg15*, *Iftm3* and *Il6* mRNA, normalized to *Rn18s* rRNA, at 16 hours post IAV challenge in WT and Δ WD independent lung slices from 6 mice. Mann Whitney U test: $*p < 0.05$ $n = 7$ WT, $n = 5$ Δ WD.

To analyze IAV entry into MEFs early in infection, we performed *in vitro* assessments of viral entry to confirm our previous work that the WD domain of ATG16L1 slows endocytosis and nuclear entry of IAV [18]. We used two antibodies to distinguish between internal (HA1 Ab) and external virus (PINDA Ab). External HA epitopes were masked using PINDA, and then cells were permeabilized and internalized virus was identified using HA1 Ab [28]. There was an increased frequency of internalized particles (green only puncta) in Δ WD MEFs cells (Figure 2A), indicating increased endocytosis of IAV into Δ WD MEFs at 30 min. WGA stained both the cell membrane and the nucleus after fixation. No detectable puncta were observed in cells not infected with IAV but subjected to the staining procedure. A control using pre-treatment with Dynasore, a noncompetitive reversible inhibitor of dynamin that inhibits endocytosis showed a distinct lack of green puncta, signifying internalized virus (Figure 2A). This suggested the WD domain has a role that provides a protective benefit to the cell membrane against viral entry by endocytosis.

In parallel experiments IAV nucleoprotein (vRNP) import into the nucleus was monitored by immunostaining for NP [28]. A semi-quantitative estimate of delivery of vRNPs to the nucleus determined by subtracting background staining

demonstrated differences in time frame of nuclear localization in the two cell lines (Figure 2B). Distinct vRNP localization to the nuclei was increased in Δ WD MEFs at 2 h compared to 4 h for WT MEFs. Corrected total nuclear fluorescence (CTNF) calculations were markedly greater for Δ WD values compared with WT MEFs at 2 h and 3 h. At 2 h NP was virtually absent from the nucleus of WT MEFs, however by 5 hpi values between WT and Δ WD were not statistically different (Figure 2B). This suggests that in the initial stages of IAV infection, entry is increased in Δ WD MEFs compared to WT MEFs, confirming previously published results (18). However, quantitative PCR (qPCR) analysis of viral RNA over this early time course from 4–12 hpi showed that there was a clear increased replication of IAV in WT cells compared with Δ WD cells. Genome replication was evident by 6 hpi, with elevated levels of IAV RNA in WT cells than Δ WD cells for every time point up to 12 hpi (Figure 2C). However, secretion of virus from Δ WD lung explants overtook that of WT explants from 24 to 72 hpi, as measured by plaque assay (Figure 1B).

To explain these results, we measured *Ifnb1/Ifn β 1* mRNA levels at homeostasis in WT and Δ WD MEFs by qPCR and showed that basal levels of *Ifnb1* mRNA were raised in Δ WD MEFs, suggesting a constitutive, low-level production of

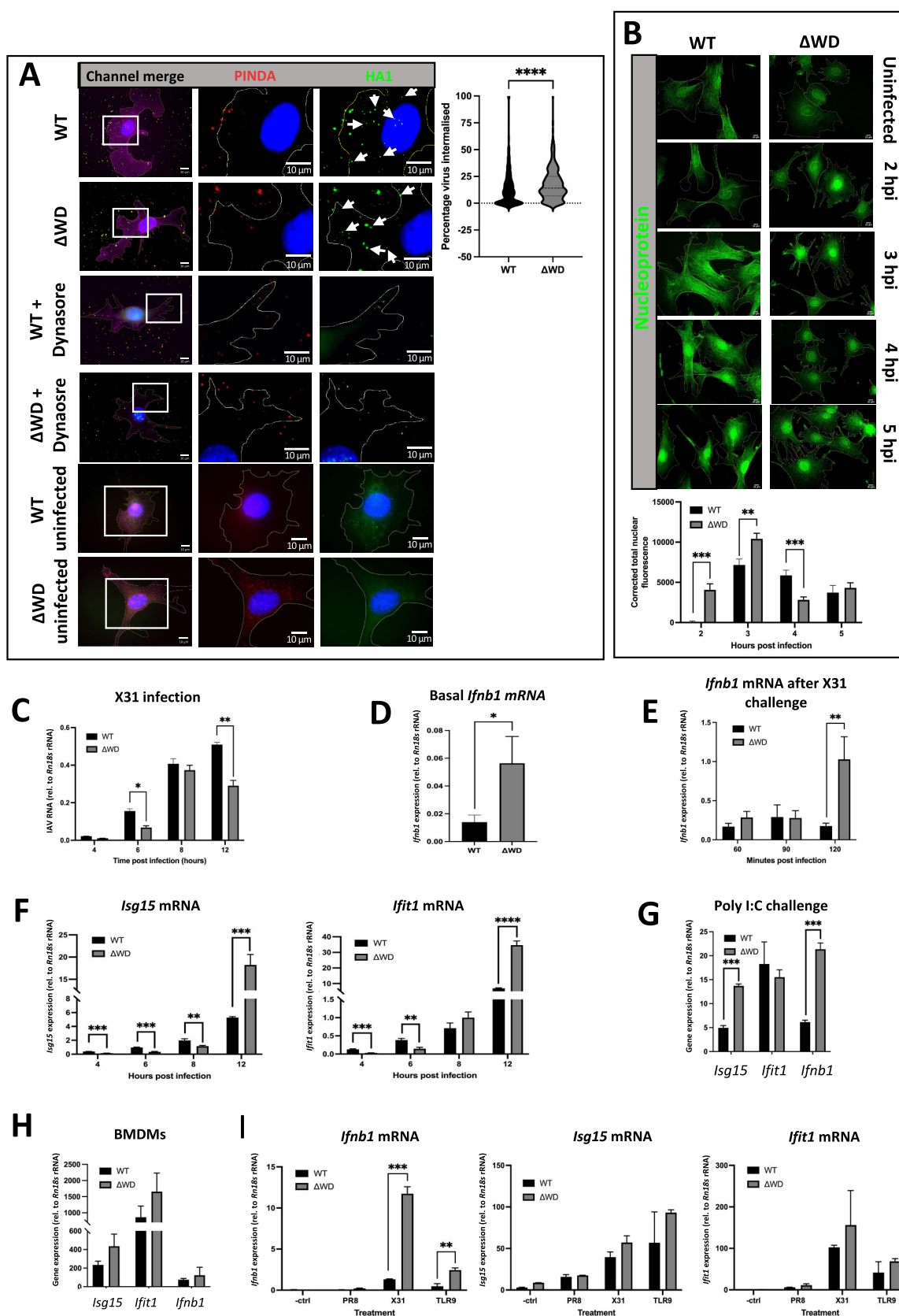


Figure 2. ATG16L1 WD domain slowed IAV entry and attenuated cytokine responses at homeostasis and following IAV and dsRNA challenge. (A) IAV was bound to WT and ΔWD MEF cells for 60 mins on ice before internalization at 37 °C for 30 mins. Red puncta stained with PINDA showed external virus, green puncta stained with HA1 showed internalized virus (white arrows) and yellow showed double stained external virus which were identified by the spot detection algorithm using CellProfiler. Controls included incubation with 80 μm dynasore, a noncompetitive reversible inhibitor of dynamin, for 30 mins, and uninfected mock control. Cells were counterstained with WGA at 647 nm to show plasma membrane (magenta) and DAPI for nuclei (blue). Percentage of virus internalized per cell is presented as a violin plot. A Mann-Whitney U test was performed: **** = $p < 0.0001$. Cell numbers counted were 837 WT and 417 ΔWD cells, analyzed across 3 independent coverslips. (B) WT and ΔWD cells were infected with IAV X31 over a time course of 0–5 hpi, fixed and stained with anti-np antibody (green). The graph shows the

Ifnb1/Ifnb1 mRNA in the absence of the WD domain (Figure 2D). As this transcript is normally rapidly turned over, it indicates persistent signaling or decreased suppression in Δ WD cells. This raised the possibility that the WD domain of ATG16L1 suppresses IFN signaling pathways in WT cells. Assessment of *Ifnb1/Ifnb1* mRNA production following infection of WT and Δ WD MEFs with IAV showed similar induction of *Ifnb1/Ifnb1* mRNA in both cell types during the first 90 minutes, but there was a dramatic 5-fold increase in *Ifnb1/Ifnb1* transcription at 120 min in Δ WD MEFs compared to controls (Figure 2E). This rise in *Ifnb1/Ifnb1* mRNA at 2 h may promote antiviral responses absent from WT cells and explain the decreased replication of IAV genomes seen in Δ WD compared to WT controls up to 12 hpi. We analyzed expression of interferon stimulated genes (ISGs) that are downstream of IFNB/IFNB1 signaling and that inhibit viral RNA and protein synthesis as well as enhance virus degradation. *Isg15* and *Ifit1/Isg56* (interferon-induced protein with tetratricopeptide repeats 1) mRNA expression were detected 12 h post infection with levels of *Isg15* and *Ifit1/Isg56* mRNA 5-fold greater in Δ WD MEFs compared to WT controls (Figure 2F).

Further experiments to elucidate signaling pathways used poly I:C as a potent dsRNA mimic and TLR3 agonist [29] to investigate differences in IFN signaling between Δ WD and WT MEFs (Figure 2G) as well as innate immune cells such as bone marrow-derived macrophages (BMDMs) (Figure 2H). Responses in BMDMs were 100-fold greater than MEFs. In both MEFs and BMDMs induction of *Ifnb1/Ifnb1* and *Isg15* mRNA after poly I:C stimulation was greater in Δ WD cells compared to WT cells (Figure 2F), but the difference only reached statistical significance in MEFs. These results show that the WD domain of ATG16L1 suppressed IFN signaling in epithelial cells and bone marrow-derived macrophages, not only in response to viral infection, but also to dsRNA. Increased *Ifnb1/Ifnb1*, *Isg15*, and *Ifit1* mRNA expression in BMDMs from Δ WD cells was also seen with the TLR9 ligand (Figure 2I). Interestingly, IAV strain PR8 did not illicit the same cellular response as IAV X31 (Figure 2I), which has been observed by others in a comparative study on the IAV isolates [30].

We next investigated the antiviral sensors involved in induction of interferon. TLR3 recognizes dsRNA in endosomes, where activation results in downstream induction of IFN regulatory factors (IRFs), ultimately initiating IFN, ISG and cytokine expression. When TLR3 was inhibited by treatment with a direct, competitive and high affinity inhibitor,

there was decreased poly IC-stimulated *Ifnb1/Ifnb1* mRNA and *Isg15* mRNA expression in both WT and Δ WD cells (Fig S1A). RIGI/RIG-I is a cytoplasmic receptor that senses RNA with 5'-tri- or diphosphate at their terminus. Knockout of *Rigi* expression was confirmed by reduced protein production, determined by western blot, in the WT *rigi* KO #2, and Δ WD *rigi* KO #1 and #2 cell lines (Fig S1B). WT *rigi* KO #2 and Δ WD *rigi* KO #2 cells were infected with IAV for 120 min, and *Ifnb1/Ifnb1* mRNA was measured by qPCR (Fig S1C). Lack of RIGI/RIG-I protein did not affect levels of *Ifnb1/Ifnb1* mRNA, in fact, it appeared to lead to an increase in *Ifnb1/Ifnb1* mRNA levels in both WT KO cells and Δ WD KO cells compared to WT and Δ WD cells where functional RIGI/RIG-I was present. Interestingly, when TLR3 was inhibited, there was an attenuation in *Ifnb1* mRNA production following IAV infection in both WT and Δ WT cells (Fig S1C). These results suggested that the IAV-induced interferon signaling was generated through TLR3 activation in the endosome and not by RIG-I activation in the cytoplasm, indicating an increased entry of IAV by endocytosis for this immune signaling pathway to be triggered, which supports the increased endocytosis entry into Δ WD cells reported in Figure 2A.

Exogenous cholesterol reversed the enhanced entry of IAV in Δ WD cells

The composition of lipid membranes regulates the entry of many viruses into cells, and it has been reported that complete loss of ATG16L1 resulted in intracellular cholesterol accumulation [26,27]. The next experiments explored the possibility that loss of the WD and linker domains affected cholesterol localization resulting in increased entry of IAV. Uptake with the acid bypass technique was used to follow the ability of IAV to fuse with the plasma membrane. Virus was incubated with cells at 4°C to allow binding to the plasma membrane in the absence of endocytosis. Cells were then warmed to 37°C in media at pH 5.0 to induce direct fusion of the virus with the plasma membrane and entry of viral RNA genomes was assessed by staining of viral NP in the nucleus. A representative image shows increased NP in the nucleus of Δ WD cells compared to control at 30 min following acid bypass [31] in WT and Δ WD cells (Figure 3A). The frequency of nucleoprotein (NP) puncta during a 10–50 min infection at pH5 following acid bypass in Δ WD MEFs showed a significant increase in intracellular NP frequency in Δ WD MEFs. These increases were not seen in control experiments

average corrected total nuclear fluorescence determined for each cell nuclei (+SEM). A Mann-Whitney U test was performed: ** $p < 0.01$ *** $p < 0.001$, 30 cells were analyzed across 4 independent coverslips. (C) Relative quantity of IAV X31 viral RNA (+SEM) in WT and Δ WD cells over a time course of 4 to 12 hpi by qPCR. Independent samples t-test performed: * $p < 0.05$ ** $p < 0.01$. $n = 3$. (D) Basal expression levels of *Ifnb1* mRNA (+SEM) in uninfected WT and Δ WD MEFs, relative to *Rn18s* rRNA measured by qPCR. Mann Whitney U test performed: * $p < 0.05$ $n = 5$. (E) *Ifnb1* mRNA expression relative to *Rn18s* rRNA after 0–120 mins time course of IAV infection in WT and Δ WD MEFs. Mann Whitney U test: ** $p < 0.005$. Independent samples t-test: *** $p < 0.001$. $n = 3$. (F) *Isg15* and *Ifit1* mRNA expression levels (+SEM) relative to *Rn18s* rRNA after 0–12 h infection with IAV X31 in WT and Δ WD MEFs. Independent samples t-test: *** $p < 0.005$. Independent samples t-test: *** $p < 0.001$. $n = 3$. (G) *Isg15*, *Ifit1* and *Ifnb1* mRNA expression levels relative to *Rn18s* rRNA in MEFs from WT and Δ WD mice treated with poly I:C (dsRNA) for 4 h, measured by qPCR. Independent samples t-test: *** $p < 0.001$. $n = 3$. (H) *Isg15*, *Ifit1* and *Ifnb1* mRNA expression levels relative to *Rn18s* rRNA in BMDMs from WT and Δ WD treated with dsRNA for 4 h, measured by qPCR. Independent samples t-test performed: no significant comparisons detected. $n = 3$. (I) *Ifnb1*, *Isg15* and *Ifit1* mRNA levels relative to *Rn18s* rRNA in BMDMs infected with IAV PR8 or IAV X31 for 4 hpi, or treated with TLR9 ligand (5 μ m) for 4 h. Independent samples t-test: ** $p < 0.01$. *** $p < 0.001$. $n = 3$.

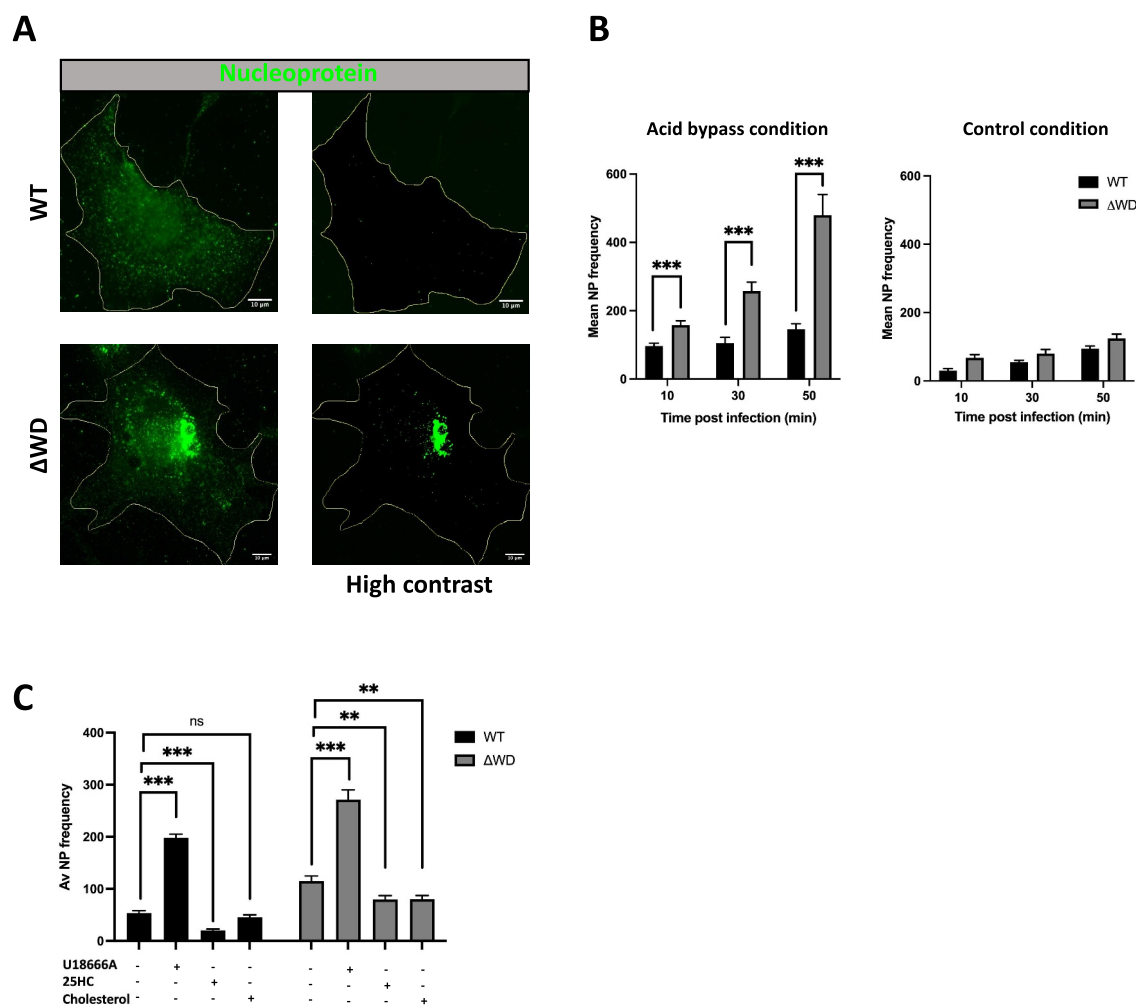


Figure 3. WD domain of ATG16L1 slowed fusion of IAV to the plasma membrane. (A) Time course of nucleoprotein puncta frequency (+SEM) in WT and ΔWD MEFs of IAV NP at 30 mins using mouse anti-np and anti-mouse secondary 488. (B) Graphs show a time course of frequency (+SEM) of NP puncta in WT and ΔWD MEFs at 10, 30 and 50 mins MEFs cells following acid fusion at pH5 and or control pH7. Mann Whitney U test: $***p < 0.001$, 50 cells analyzed across 3 independent experiments. (C) Nucleoprotein puncta frequency (+SEM) in WT and ΔWD MEFs cells at 50 mins post infection after pre-treatment with U18666A (3 μg/mL) for 24 h, or 25 hydroxy cholesterol (5 μm) for 16 h or cholesterol (80 μm) for 12 h as indicated. Mann Whitney U test: $***p < 0.001$, $**p < 0.01$.

carried out at pH 7 which prevents fusion with the plasma membrane (Figure 3B). The next experiment tested whether changes in cholesterol at the plasma membrane resulting from the loss of the WD domain could influence fusion of IAV. This was tested by pharmacologically altering plasma membrane cholesterol concentration. U18666A is a cationic sterol that inhibits Niemann-Pick C1 (NPC1) protein. Inhibition of NPC1 slows movement of cholesterol from late endosomes and lysosomes and depletes cholesterol at the plasma membrane [32]. 25HC is an oxysterol and metabolite of cholesterol found in the plasma membrane that interferes with viral infection via multiple pathways, including viral entry by inhibiting membrane fusion [33–35]. Cells were pre-incubated with either U18666A, 25HC or cholesterol, before drug-containing media was removed, and IAV uptake was tested by acid fusion at pH 5 (Figure 3C). Frequency of NP puncta within WT cells and ΔWD MEFs was substantially increased when cells were pre-incubated with U18666A, suggesting cholesterol depletion at the plasma membrane enhanced

fusion. In contrast, addition of cholesterol and 25HC decreased NP frequency in both cell genotypes (Figure 3C). Of note, supplementation of the cells with exogenous cholesterol resulted in a lower internalized NP frequency in ΔWD MEFs, showing that the increased entry of IAV seen in ΔWD cells was reversed by adding cholesterol.

Changes in intracellular cholesterol localization in cells lacking the ATG16L1 WD domain

The acid bypass experiments showed that depletion of cholesterol from the plasma membrane of WT MEFs mimicked the effects of loss of the WD domain on IAV fusion. Given that previous studies have shown that loss of the entire ATG16L1 protein leads to an accumulation of cholesterol in the cytoplasm [26], we tested whether cholesterol accumulation may also occur following loss of the WD and linker domains. Confocal microscopy of cells stained with filipin III to detect endogenous cholesterol, or on cells transfected

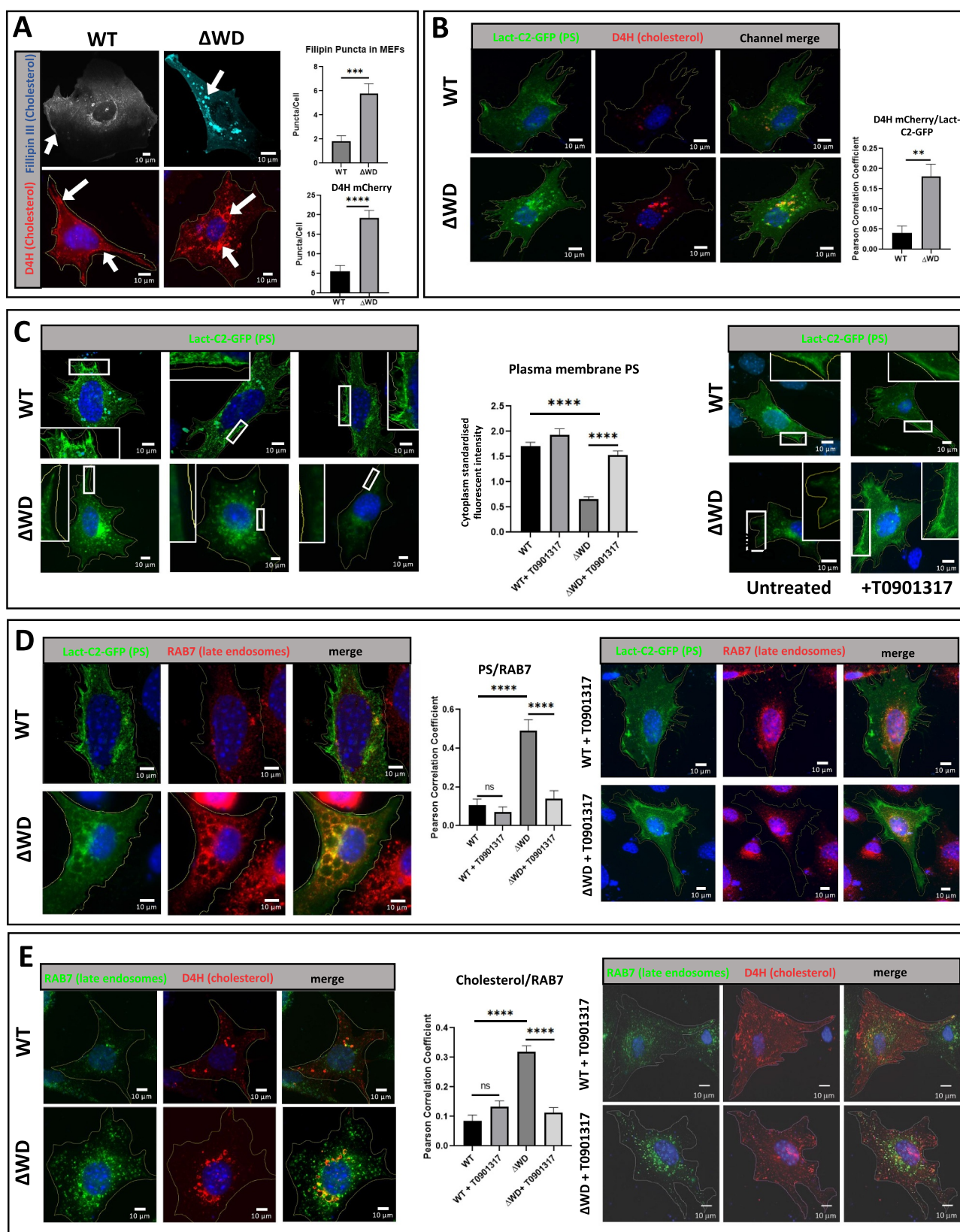


Figure 4. Intracellular cholesterol and phosphatidyl serine (PS) accumulated in late endosomes in MEFs lacking the WD domain. (A) Increased size and frequency of cholesterol aggregation in Δ WD MEFs. WT and Δ WD MEFs were fixed and stained with filipin III or transfected with a plasmid encoding D4H mCherry for 24 hours before fixing and staining with DAPI and viewed by Zeiss LSM980-airyscan confocal microscope. White arrows show cholesterol at plasma membrane in WT and intracellular aggregation in Δ WD. Top graph: filipin puncta per cell in WT and Δ WD MEFs stained with filipin were imaged in the 358 nm channel of a LSM 980 airyscan 2 confocal microscope. Individual puncta in individual cells for each group were counted by hand in Zen2 software. Unpaired T-test of each group's mean puncta count per cell (WT $N = 12$, Δ WD $N = 14$) using GraphPad Prism software. Bottom graph: D4H mCherry puncta per cell (+SEM). Mann Whitney U test: $*p < 0.05$, $n = 10$. (B) Increased phosphatidylserine (PS) and cholesterol in cytoplasmic puncta in Δ WD MEFs. WT and Δ WD MEFs were transfected with D4H mCherry and PS biosensor lact-C2-gfp plasmids for 24 hours before fixing and imaging. Graph shows number of double-positive puncta (+SEM). Mann Whitney U test performed: $**p < 0.01$, $n = 8$. (C) PS loss from plasma membrane in Δ WD MEFs was restored following treatment with T0901317. Untreated (left panel images) and T0901317 treated

with D4H mCherry, a plasmid expressing a modified domain 4 of perfringolysin O that effectively binds cholesterol in intracellular membranes [36] showed large perinuclear puncta in the cytoplasm of Δ WD MEFs (Figure 4A). In contrast these large puncta were absent from WT cells, where filipin III and D4H cherry localized at the plasma membrane and in small cytoplasmic puncta (Figure 4A). The location of phosphatidylserine (PS), which is essential for maintaining and stabilizing cholesterol in the inner leaflet of the plasma membrane [37,38], was detected using the PS biosensor Lact-C2-GFP (Figure 4B) and showed significantly more colocalization with cholesterol in intracellular puncta in Δ WD cells than in WT cells. This was supported by Pearson correlation analysis which determined a 3-fold increase in colocalization between PS and cholesterol in Δ WD MEFs compared to WT MEFs (Figure 4B). Lact-C2-GFP localized to the plasma membrane and cytoplasmic puncta in WT cells (Figure 4C). In contrast, Lact-C2-GFP staining at the plasma membrane was noticeably reduced in Δ WD MEFs (Figure 4C). These data suggested that loss of the ATG16L1 WD domain disrupts intracellular cholesterol homeostasis leading to reduced cholesterol and PS at the plasma membrane and retention of cholesterol and PS within intracellular vesicles in Δ WD MEFs. Cells were treated with T0901317, which is an agonist of the transcription factor NR1H/liver X receptor and increases ABCA1 transporter expression [39]. Upregulation of ABCA1 on endosomal membranes facilitates active transport of cholesterol out of cells as esterified cholesterol. We show here that treatment of Δ WD cells with T0901317 restored PS to the plasma membrane (Figure 4C).

The distribution of cholesterol and PS in endosome compartments was analyzed by immunostaining for RAB7, which in its active (GTP) form binds to the cytoplasmic face of late endosomes. Analysis of WT and Δ WD MEFs using the Lact-C2-GFP probe for PS showed colocalization of PS with RAB7 in cytoplasmic puncta and as shown above, the PS staining at the plasma membrane was significantly diminished in Δ WD cells (Figure 4D). Interestingly, the vesicles containing LacC2 and RAB7 in Δ WD MEFs were larger and swollen compared to WT cells. Quantitative assessments revealed a correlation between PS and RAB7 that is 4.5-fold greater in Δ WD MEFs than WT cells and indicates that more PS is found in late endosomes in cells lacking the ATG16L1 WD domain. Incubation of Δ WD cells with T0901317 markedly reduced numbers of puncta double positive for RAB7 and Lact-C2-GFP (Figure 4D). The Pearson coefficients showed that T0901317 reduced colocalization of PS with RAB7 by 3.5-fold in Δ WD cell and restored PS levels at the plasma membrane (Figure 4D).

Moreover, vesicles containing cholesterol visualized using the D4H mCherry probe and RAB7 in Δ WD MEFs were also larger and swollen compared to WT cells (Figure 4E). The colocalization of D4H mCherry and RAB7 was 3.7-fold greater in Δ WD MEFs than WT cells, demonstrating that cholesterol is significantly more abundant in late endosomes of cells lacking the ATG16L1 WD domain. In summary, in cells lacking the WD domain of ATG16L1, PS and cholesterol redistribute from the plasma membrane to late endosomes containing RAB7. T0901317 treatment resulted in a markedly reduced frequency of RAB7 and D4H mCherry double-positive puncta staining in Δ WD cells (Figure 4E). Pearson coefficients suggested colocalization in vesicles to be reduced 2.8-fold by T0901317 suggesting that the drug caused loss of cholesterol from late endosomes/lysosomes in Δ WD cell. T0901317 had little effect on WT MEFs apart from a small non-statistically significant ($p = 0.2156$) increase in D4H mCherry and RAB7 colocalization. Experiments comparing localization of cholesterol in lysosomes and early endosomes in WT and Δ WD cells showed partial colocalization of D4H cholesterol probe with LAMP1-positive lysosomes, but very little colocalization with EEA1-positive early endosomes (Figure 5A). Taken together, these results indicated that altered cholesterol and PS transport in Δ WD cells results in loss of cholesterol from the plasma membrane and increased cholesterol in lysosomes and late endosomes, but not in early endosomes, which are derived from membrane recycled from the plasma membrane.

Loss of ATG5 and ATG12 also leads to cholesterol accumulation in lysosomes [26]. This accumulation is independent of canonical autophagy because cholesterol distribution is not altered in cells lacking ATG3, ATG9 and ATG14 which act upstream of ATG12–ATG5 [26]. This makes it possible that WD domain-dependent conjugation of LC3 to membranes regulates cholesterol and PS transport. The distribution of PS and LC3 were therefore studied in cells incubated with chloroquine to raise vacuole pH to activate CASM and LC3 conjugation to endo-lysosome membranes. In WT cells chloroquine induced the formation of swollen vesicles containing PS and many were positive for LC3 (Figure 5B). This is consistent with current models where cholesterol released from lipid droplets delivered to lysosomes by autophagy remains trapped in the lysosome because export from the vacuole through Niemann-Pick type C (NPC) transporters requires low pH [40,41]. Vesicles containing PS were also present in cells lacking the WD domain, again suggesting that PS accumulates because NPC transporters are inhibited by raised pH, but these vacuoles were negative for LC3 (Figure 5B). This suggests that WD-dependent conjugation of LC3 to vacuole membranes does not play a major role in

(right panel images) WT and Δ WD MEFs were transfected with the lact-C2-gfp plasmid for 24 hours. White boxes are enlarged plasma membrane from image. Right panel shows WT and Δ WD cells treated with T0901317 for 24 h before fixing and staining with DAPI. Cytoplasm standardized fluorescent intensity of membrane is shown in graph (+SEM). Mann Whitney U test performed: **** $p < 0.0001$ $N = 8$. (D) PS accumulates in large RAB7-positive cytoplasmic vesicles in Δ WD cells and restored to plasma membrane by T0901317 treatment. Untreated (left panel images) and T0901317 treated (right panel images) WT and Δ WD MEFs were transfected with the lact-C2-gfp plasmid for 24 hours before fixing and staining with anti-rab 594. PS is seen with Rab7 in large vesicles of untreated Δ WD cells. T0901317 drug treatment significantly reduces Δ WD MEF PS-GFP/Rab7 puncta in Δ WD and restores plasma membrane staining. Graphs quantify PS/RAB7 colocalized puncta (+SEM). Mann Whitney U test performed: **** $p < 0.0001$ WT $n = 9$, Δ WD $n = 8$. (E) Intracellular cholesterol accumulation in Δ WD MEFs is reversed following treatment with T0901317. Untreated (left panel images) and T0901317 treated (right panel images) WT and Δ WD MEFs were transfected with the D4H mCherry plasmid and stained with anti-RAB7 488. Graphs quantify D4H mCherry/RAB7 colocalized puncta (+SEM). Mann Whitney U test performed: **** $p < 0.0001$ $n = 8$.

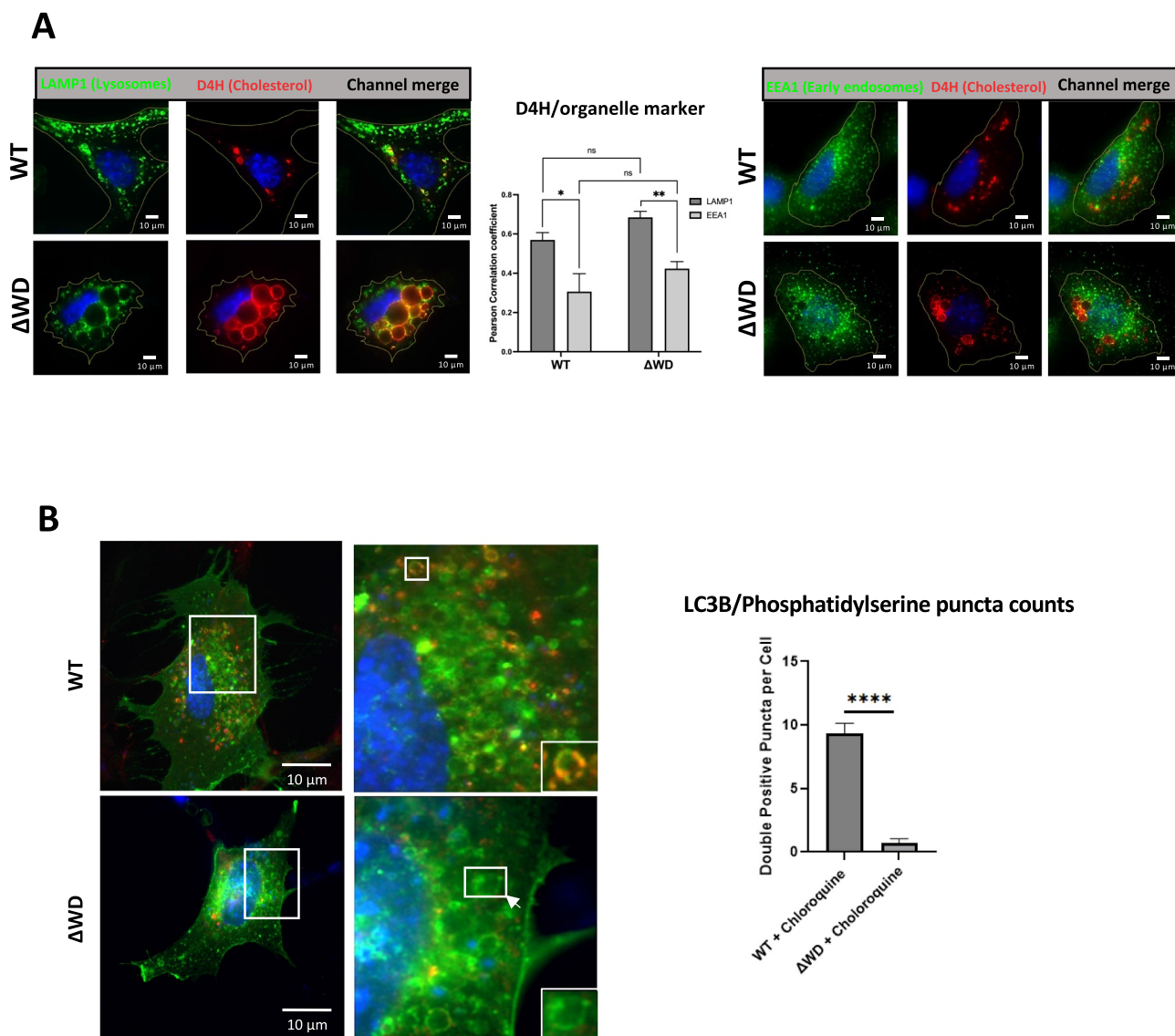


Figure 5. The Δ WD mutation impaired the localization of LC3 to PS/cholesterol vesicles. (A) Distribution of lysosomes and early endosomes with cholesterol in WT and Δ WD cells. Cells were transfected with D4H and immunostained with either LAMP1 or EEA1 antibodies. Pearson correlation coefficients of D4H mCherry colocalization with LAMP1 or EEA1 are presented on the graph (+SEM). Mann Whitney U test performed: ** $p < 0.01$, $n = 14$. (B) WT and Δ WD MEFs transfected with lact-C2-gfp were treated with chloroquine (50ug/ml) for 2 h before fixing in methanol and staining with mouse anti- LC3B antibody with anti-mouse 594 secondary antibody (red). Bar chart shows counts of LC3b/Lact-C2-gfp double-positive intracellular puncta after chloroquine treatment of WT and Δ WD MEFs for 2 h. Puncta counted using ImageJ, with graphing and statistical analysis (unpaired T-test) using GraphPad prism (WT $N = 10$, Δ WD $N = 11$).

determining PS and cholesterol distribution. This raises the possibility that the WD domain may function at other sites in cholesterol transport possibly modulating non-vesicular lipid transport mediated by lipid transfer proteins and OSBP (oxysterol binding protein)-and OSBPL proteins. OSBP mediates cholesterol transfer from the endoplasmic reticulum to lysosomes at membrane contact sites [42] and reverse transfer to the ER is facilitated by OSBPL1A/ORP1 and OSBPL5/ORP5 [43].

Cholesterol is reduced in the plasma membrane of Δ WD cells and tissues

In the next series of biochemical experiments, we used sub-cellular fractionation of MEF cells isolated from WT and Δ WD mice to analyze cholesterol levels in the plasma

membrane. In the initial lysate, there was no significant difference in the total amount of cellular cholesterol or unesterified cholesterol between WT and Δ WD MEF cells (Figure 6A). Cells were then fractionated by density gradient centrifugation and the plasma membrane was identified by immunoblotting for ITGB1/ β 1-integrin (Figure 6B). Fractions containing the highest levels of ITGB1 across the gradient were analyzed for cholesterol content and normalized to protein concentration. There was significantly less cholesterol and unesterified cholesterol in plasma membrane of Δ WD MEFs compared to WT MEFs (Figure 6C).

The effect of loss of the ATG16L1 WD domain on cholesterol distribution in tissues *in vivo* was tested by analyzing membrane fractions isolated from brain tissue from Δ WD and WT mice. Interestingly, measurement of total cholesterol (Figure 6D) showed that there were significantly higher levels

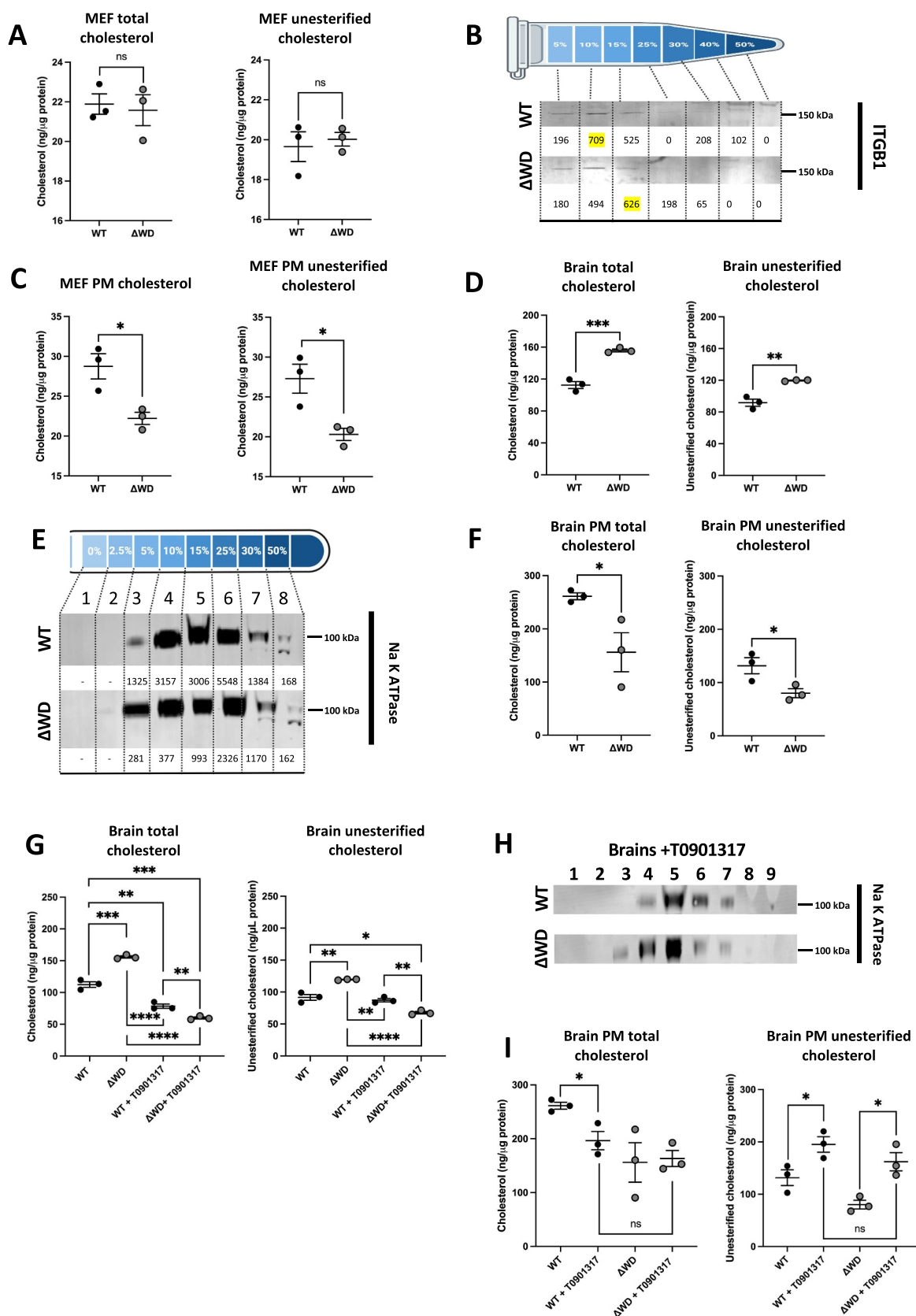


Figure 6. Plasma membrane in brains of mice lacking WD domain of ATG16L1 were deficient in cholesterol. (A) Total and unesterified cholesterol was quantified from MEF lysates using the Amplex Red cholesterol assay, and normalized to the protein concentration of the WT and ΔWD samples (\pm SEM). Independent samples t-test performed: ns = $p > 0.05$ $N = 3$. (B) Western blot showing MEF cells following fractionation by ultracentrifugation on a 2.5–50% Nycodenz-sucrose gradient and the plasma membrane (PM) fractions identified by ITGB1/ β 1 integrin western blot, quantified on ImageJ (numbers below respective band). (C) Total and unesterified cholesterol was quantified from MEF PM fractions, identified in Fig 6B. Graphs report cholesterol concentration normalized to protein concentration of WT and ΔWD samples (\pm SEM). Independent samples t-test performed: * $p < 0.05$ $n = 3$. (D) total and unesterified cholesterol was quantified from brain tissue lysates. Graphs report cholesterol concentration normalized to protein concentration of WT and ΔWD samples (\pm SEM). Independent samples t-test performed: ** $p < 0.01$, *** $p < 0.001$ $n = 3$. (E) Western blot showing brain tissue following fractionation by ultracentrifugation on a 2.5–50% step Nycodenz-sucrose gradient and the plasma membrane

of cholesterol in the brains of Δ WD mice compared to littermate controls. Analysis of cholesterol esterification revealed that this increase in total cholesterol was due predominantly to increases in unesterified cholesterol. Brain tissue from WT and Δ WD mice were homogenized and fractionated on a 2.5–50% Nycodenz-sucrose step gradient to separate plasma membrane (Figure 6E). Plasma membrane fractions were identified by presence of sodium-potassium ATPase, and fractions with the peak levels of sodium-potassium ATPase labeling relative to protein concentration were assayed for total and unesterified cholesterol. These results demonstrated that, despite higher levels of total cholesterol in the tissue, the concentration of plasma membrane cholesterol was reduced in Δ WD brain tissue (Figure 6F). This was consistent with the *in vitro* results obtained from Δ WD MEFs.

WT and Δ WD mice were treated for 3 days with T0901317 to promote cholesterol efflux from cells. As recorded above, the brains of untreated Δ WD mice showed greater levels of total and unesterified cholesterol compared to untreated WT controls (Figure 6G). Treatment with T0901317 significantly decreased cholesterol in WT and Δ WD brain tissue, with T0901317-treated Δ WD brain significantly lower than untreated and treated WT brain. Treated brains from WT mice showed no difference from untreated for unesterified cholesterol levels, whereas unesterified cholesterol was significantly decreased in treated Δ WD mice to below the level of that found in treated WT mice (Figure 6G). These results suggest that the drug treatment mainly leads to the efflux of unesterified cholesterol in Δ WD mice. The brains of treated mice were fractionated on 2.5–50% Nycodenz step gradient and plasma membrane fractions identified by Na/K ATPase labeling as above (Figure 6H). As shown in cell culture, WT mice contained higher levels of total and unesterified cholesterol in the plasma membrane of brain tissue compared to Δ WD mice. T0901317 treatment slightly lowered levels of total cholesterol in the plasma membrane fractions from WT brains (Figure 6I) and total cholesterol was not altered in the plasma membrane in brains of Δ WD mice treated with T0901317. Importantly, however analysis of unesterified cholesterol showed that T0901317 increased levels of unesterified cholesterol at the plasma membrane in both WT and Δ WD brain tissue. After drug treatment there was no significant difference in unesterified cholesterol levels between treated WT and Δ WD brain plasma membrane. Taken together, these data demonstrate a distinct reduction of cholesterol at the plasma membranes of Δ WD MEFs as well as within brain tissue. The cholesterol efflux-promoting drug T0901317 increased levels of unesterified

cholesterol in the plasma membrane of brains of both genotypes, and restored levels of unesterified cholesterol in the plasma membrane of Δ WD mice to levels seen in untreated WT controls.

Discussion

Our study reveals a new unconventional role for the WD40 domain of ATG16L1 in the control of cholesterol distribution, plasma membrane integrity and influenza virus infection. Our previous study on the ATG16L1 protein reported that the WD and linker domains are essential in restricting lethal influenza infection [18]. We show here that absence of the WD domain resulted in increased IAV fusion and endocytosis, increased the frequency of IAV vRNP import into the nucleus. By 16 hpi, there was a significant increase in cytokine expression in IAV-infected lung explants of Δ WD mice, followed 3 days after with increased secreted virus. Challenge of Δ WD MEFs with IAV increased early IFN β /IFN β expression by 2 hpi and ISGs by 12 hpi. Ligands for TLR3 and TLR9 also stimulated a greater increase in IFN and ISG expression in Δ WD BMDMs and MEFs after 4 hours. Addition of cholesterol and 25-OH cholesterol reversed the increased import of vRNPs in Δ WD cells, whereas depletion of cholesterol from the plasma membrane of WT MEFs with U18666A mirrored the effects of loss of the WD domain. We found a prominent accumulation of cholesterol in a perinuclear compartment identified as late endosomes, supporting a previously described role for the WD domain of ATG16L1 in regulation of lipid transport [26,27], controlling the transport of cholesterol and PS from late endosomes and lysosomes to the plasma membrane. Pharmacological treatment with T0901317 to upregulate the ABCA1 cholesterol transporter restored the recruitment of both cholesterol and PS from the intracellular puncta to the plasma membrane. RAB7 staining identified the intracellular puncta as late endosomes, consistent with the finding that ATG16L1 promotes lysosome exocytosis to promote plasma membrane repair through a RAB7 late endosome pathway [26]. Changes in cholesterol distribution were also observed “*in vivo*” where there were higher cholesterol levels in the brains of mice lacking the WD and linker domains, and, as seen in cell culture, there was a deficiency of cholesterol in the plasma membrane of brain tissue. The WD domain of ATG16L1 plays a crucial role during CASM-mediated conjugation of LC3 to endo-lysosome compartments in response to raised luminal pH. The mouse used in this study lacks CASM [10,18] making it possible that CASM may influence cholesterol distribution between endosomes and the plasma

fractions identified by Na/K ATPase beta subunit western blot, quantified on image J (numbers below respective band). (F) Total and unesterified cholesterol was quantified from brain PM fractions, identified in Figure 6E. Graphs report cholesterol concentration normalized to protein concentration of WT and Δ WD samples (\pm SEM). Independent samples t-test performed: * = $p < 0.05$ $n = 3$. (G). Total and unesterified cholesterol was quantified from brain tissue lysates of mice treated or untreated with T0901317 for 3 days. Graphs report cholesterol concentration normalized to protein concentration of WT and Δ WD samples (\pm SEM). Independent samples t-test performed: * $p < 0.05$, ** $p < 0.01$, *** $p < 0.001$, **** $p < 0.0001$ $n = 3$. (H) Western blot showing brain tissue following treatment of mice with T0901317 for 3 days, fractionated on a 2.5%–50% Nycodenz-sucrose gradient and the plasma membrane fractions identified by ATP1B/Na⁺/K⁺ ATPase beta subunit western blot. (I) Total and unesterified cholesterol was quantified from brain PM fractions of mice treated or untreated with T0901317 for 3 days. Graphs report cholesterol concentration normalized to protein concentration of WT and Δ WD samples (\pm SEM). Independent samples t-test performed: * = $p < 0.05$.

membrane. The Δ WD mouse described in this paper does not allow us to exclude a role for CASM and dissecting the precise role played by CASM will require further experiments such as specific inhibition of CASM by expression of Sop-F [14] or studying the effects of point mutations that affect binding of the WD domain to the V1H subunit of the V-ATPase [10,15,16]. The WD and linker domains may function at other sites in cholesterol transport possibly modulating non-vesicular lipid transport mediated by lipid transfer proteins and oxysterol binding protein (OSBP)-and OSBP-related proteins (ORPs). OSBP mediates cholesterol transfer from the endoplasmic reticulum to lysosomes at membrane contact sites [43]. Interestingly, RAB7 is recruited to phagosomes and required for phagolysosome maturation. However, in cholesterol-loaded cells, RAB7 is inactive with accumulation of unesterified cholesterol in endo-membranes which prevents their fusion with lysosomes [44]. This may suggest that there may be an impairment of RAB7 activation in cells lacking the WD domain, where there is an accumulation of cholesterol in late endosomes. Cells also transport lipids between organelles by non-vesicular pathways, including movement of cholesterol to the plasma membrane, a process that permits rapid membrane expansion of intracellular compartments, such as autophagosomes. Other WD-containing proteins such as ATG2A play a role in membrane expansion [45]. It has been well established that viral entry can be modulated by the concentration of cholesterol within the membranes of the cell-virus interaction [22]; a significant presence of cholesterol within membranes orders bilayer lipids and stabilizes the fusion intermediates to promote entry [43]. The use of methyl- β -cyclodextrin (M β CD) dependent depletion of cholesterol has delineated the requirements of cholesterol for specific viruses, with HIV-1 requiring cholesterol in both viral and host membranes for efficient fusion [46,47] whereas only viral membrane cholesterol composition effected IAV fusion [48]. Here we show an enhancement of viral fusion at the plasma membrane when it is composed of less cholesterol in the absence of the WD domain. The effects on IAV entry and ISG production may be indirect, as there may be modest damage to endolysosomal compartments. While we cannot say definitively that increased viral fusion is entirely dependent on the reduced plasma membrane cholesterol, *in vitro* experiments supplementing Δ WD cells with cholesterol reduced fusion of IAV with the plasma membrane. Furthermore, treatment with U18666A, which depletes plasma membrane cholesterol, increased IAV fusion in WT cells, indicating that reduced cholesterol promotes IAV fusion. Early endosomes formed after IAV internalization from the cholesterol reduced plasma membrane may also have depleted cholesterol to promote IAV fusion. We also show that endocytosis and nuclear entry of IAV increased in cells lacking WD domain. While host membrane cholesterol M β CD depletion has been shown to not effect IAV entry [23], cholesterol depletion at the plasma membrane is reflected in early endosome membranes that promote cytoplasmic entry.

Autophagy proteins are involved in an array of immune pathways required for effective defense and normal functioning homeostasis. ATG16L1 is involved in regulating

inflammatory responses, with ATG16L1 shown to suppress type I IFN signaling [49] and induce regulatory T cells [50]. Specific ATG16L1 polymorphisms have been implicated in disease non-progression within chronically HIV-1 infected individuals, with distinct inflammatory and immune regulatory and responsiveness profiles observed [51]. Moreover, increased cytokine signaling has been demonstrated in ATG16L1 mice possessing the T300A mutation [52], which increases susceptibility for caspase cleavage of the protein, effectively removing the WD domain, suggesting it might regulate the inflammatory response. Here we show elevated basal *Ifnb/Ifn β* transcription, with levels of *Isg15* and *Ifit1* mRNA expression higher in Δ WD mice following IAV challenge. ISG15 has proinflammatory properties following viral infection [53], supporting the inflammatory profile found *in vivo* [18]. Although both RIGI and TLR3 pathways are known to be important for IFN induction by IAV [54,55], our experiments showed elevated signaling through the endosomal TLR3 pathway, providing evidence that the WD domain is protective against viral infection.

In conclusion, we show that removal of the WD and linker domains from the ATG16L1 protein causes intracellular cholesterol accumulation in late endosomes/lysosomes and reduces cholesterol at the plasma membrane. Precisely how the WD and linker domains affect cholesterol transport requires further study. It cannot be ruled out that ATG16L1 WD domain may protect cells from virus entry by an indirect manner, as its loss may cause endosomal damage. Even so, we show that IAV infection is enhanced when these domains are lost, and the increased viral entry is followed by a subsequent increase in IFN signaling, through the TLR3 receptor pathway and a modulation of IFN signaling, previously reported *in vivo* [18].

Materials and methods

Virus propagation

Influenza virus A PR8 is a mouse-adapted H1N1 strain originally derived from a human isolate. X31 is a mouse adapted H3N2 strain with the 6 internal genes of PR8 and the HA and NA derived genes from A/Aichi/2/1968. They were propagated in the allantoic cavity of 9-day-old embryonated chicken eggs at 35°C for 72 h [56] and titer determined using plaque assay on Madin-Darby canine kidney cells (MDCK) [57,58].

Reagents

The generation of Δ WD mice (*Atg16L1 Δ WD/ Δ WD*) has been described previously [9]. Mouse embryonic fibroblasts (MEFs) were procured from mice at embryonic day 13.5 and cultured in Dulbecco's Modified Eagles Medium (DMEM) with GlutaMAX (ThermoFisher 10,567,014) supplemented with 1% penicillin-streptomycin, kanamycin and 10% fetal bovine serum (Gibco 10,082,147). Bone marrow-derived macrophages (BMDMs) were generated from bone marrow isolated from femur and tibia flushed with RPMI 1640 (ThermoFisher 11,835,030). Macrophages were generated by culturing adherent cells in RPMI 1640 containing 10% FCS and CSF1/M-CSF

(R&D systems, Q3U4F9 30 ng/mL) for 6 days. Filipin III was from Sigma (F4767). TRIzol was from ThermoFisher (15596026); WGA 647 was from Invitrogen (W32466; 5 µg/mL); cholesterol was from Sigma Aldrich (C8667; 80 µM); 25-hydroxycholesterol was from Sigma Aldrich (H1015; 5 µM) TLR3 inhibitor was from Sigma-Aldrich (614310); poly I:C was from Sigma-Aldrich (P1530). *rigi* knockout (KO) cell lines were generated by infecting WT and ΔWD MEFs with custom CRISPR gRNA lentivirus transduction particles (Sigma Aldrich, MMPD0000132807 and MMPD000132808) in Opti-Minimal Essential Medium (Opti-MEM; ThermoFisher 31,985,070) supplemented with 16 µg/mL hexadimethrine bromide (Sigma-Aldrich, 107689). Selection was performed using 10 µg/mL puromycin and knockout validated by western blotting using anti-RIGI/DDX58 (Abcam, ab180675) and equal lane loading with mouse anti-ACTB/actin antibody (Ac-15; Sigma Aldrich, A5441). The Lact-C2-GFP plasmid was from Addgene (22852; deposited by Sergio Grinstein). TLR9 ligand CpG ODNs was from InvivoGen (ODN 1585).

Lung slice culture

The *ex vivo* lung tissue model has been previously described [59]. Briefly, WT and ΔWD mouse lungs were harvested and airways were inflated with 1% low melting point agarose in DMEM F12 (ThermoFisher 10,565,018) in Hanks' Balanced Salt Solution (HBSS; ThermoFisher 14,025,092) and cast in blocks of 2% agarose in HBSS for sectioning with a vibrating microtome. Slices were cut at 300 µm and incubated in DMEM F12 + penicillin-streptomycin + kanamycin, overnight at 37°C 5% CO₂ and infected with IAV as indicated.

Drug treatment

MEFs were treated with 10 µM/mL NR1H/liver X receptor agonist T0901317 (Sigma Aldrich, T0901317) diluted in complete media for 48 h prior to harvesting for ultracentrifugation at 61,725× g for 180 min. For mouse treatment, T0901317 was administered for 3 days prior to sacrifice at concentrations of 25 mg per kilogram of body weight. In tissue culture, U18666A (Cayman Chemical, 10009085) was used at 3 µg/mL for 24 hours. Cholesterol (Sigma-Aldrich, C8667) and 25-hydroxy cholesterol (25HC; Sigma Aldrich, H1015) were prepared in ethanol and used at 80 µM and 5 µM, respectively. Cells were incubated with poly I:C (Sigma Aldrich, P1530) for 4 hours. The TLR3-dsRNA complex inhibitor C18H13CIFNO3S (Sigma Aldrich 614,310) blocks dsRNA binding to TLR3 and was added one hour prior to infection or transfection. Chloroquine (50 µg/mL; Sigma Aldrich, C6628) was added to cells for 2 hours before fixing.

IAV entry assays by acid mediated bypass

We adapted methods previously published methods to force fusion of the IAV membrane to the plasma membrane [28,60]. MEFs were seeded onto coverslips (NP entry assay) or 6-well plates (IFNB assay) and grown to 75% confluency or 100% confluency respectively. Cells were infected with IAV

X31 at an MOI of 100 for the NP entry assay and 10 for the IFNβ assay. Virus was bound to MEFs for 1 hour at 4°C, unbound virus was removed via cold infection medium (DMEM, 50 mM HEPES, pH 6.8, 0.2% BSA (Sigma Aldrich, A7030)).

Cells were incubated for 2 min in FUSION medium (DMEM, 50 mM citric buffer adjusted to pH 5.0) before being cooled, washed in cold infection medium and incubated at 37°C in STOP medium (DMEM, 50 mM HEPES, 20 mM NH₄Cl, pH 7.4) for the appropriate time points. A control condition was also performed using pH 7.0 medium instead of the FUSION medium.

Endocytosis assay

High-resolution analysis of IAV entry to cells via endocytosis was measured using a previously published protocol [23,54]. IAV X31 (MOI: 10) was diluted in infection medium (DMEM, 50 mM HEPES, pH 6.8, 0.2% BSA) and used to infect MEFs at 4°C for 1 hour. Pre-treatment of cells with Dynasore (Sigma-Aldrich 324,410; 80 µM) for 30 min was used as a control. Unbound virus was removed with ice cold infection medium before bound virus was internalized in warm media at 37°C for a 30-min incubation. Cells were then fixed in 4% paraformaldehyde (PFA) after which the plasma membranes were stained (WGA 647) before cells were blocked for 30 min (1% BSA, 5% FCS, 1 × PBS). External influenza HA epitopes were immunostained with the primary antibody PINDA (made by Y. Yamauchi lab, University of Bristol) (1:500) in a blocking solution and incubated overnight at 4°C. PINDA was then stained with anti-rabbit IgG-Alexa Fluor® 594 (Abcam, ab150080; 1:1000) in blocking solution for 1 hour at room temperature. Cells were fixed again in 4% PFA and permeabilized in 0.1% Triton™X-100 (Sigma Aldrich, T8787) 1% BSA, 5% FCS, 1 × PBS (Sigma Aldrich, P4417). Cells were incubated with HA1 antibody (1:100; Yamauchi lab, University of Bristol), specific for the internalized HA1 epitope. Cells were washed and stained with the anti-mouse IgG Alexa Fluor® 488 (1:1000; Abcam, ab150105). Nuclei were stained with DAPI (1:5000) before coverslips were mounted and viewed using a Zeiss Axio Imager 2 for representative images. For automated image acquisition a 20X lens was used on a Zeiss LSM laser scanning confocal microscope, measuring over 3 independent cover slips. Images were analyzed using the CellProfiler program, with a spot detection algorithm employed for detection of puncta and categorizing them, which is detailed in (-23,54), counting 880 WT cells and 419 ΔWD. An in-house Python script was used to remove cells with no virus puncta, resulting in 837 WT cells and 417 ΔWD being used in analysis.

Nuclear entry assay

IAV was used to infect primary cells (MOI: 4) and diluted in OptiMEM (Thermo Fisher 31,985,070) WT and ΔWD MEFs were seeded onto coverslips. Virus was bound to cells at 4°C for 1 hour, then allowed to internalize through incubation at 37°C. Cells were fixed in 4% PFA at the following time points: 2, 3, 4 and 5 hpi; permeabilized with 0.1% Triton

X-100; blocked in 0.1 M glycine and 2% BSA solutions; and immunostained with anti-IAV NP (Abcam, ab20343) in 2% BSA blocking solution overnight at 4°C. Cells were then stained with IgG Alexa Fluor® 488 (Abcam, ab150105) in 2% BSA blocking solution for 2 hours at room temperature. Nuclei were stained with DAPI (Invitrogen D1036) for 10 min before being mounted and viewed using a Zeiss Axio Imager 2 microscope.

Quantitative IAV and cytokine transcription

Tissues were frozen in liquid nitrogen and homogenized using a TissueLyser (Qiagen) with TRIzol (ThermoFisher 15,596,026). Tissue culture cells were washed twice using PBS before addition of TRIzol and homogenization with a cell scraper and passage through a 23 G needle. For both tissue and cells, TRIzol-chloroform extractions were further purified by RNeasy MinElute Cleanup Kit (Qiagen 74,204) according to the manufacturer's instructions. RNA was analyzed by quantitative PCR (qPCR) using SYBR Green (Applied Biosystems 10,187,094) and the 7500 Standard Real-Time PCR System (Applied Biosystem) with Qiagen primer sets. IAV primers were the M forward primer 5'GACCRATCCTGTACCTCTGAC 3' and M Reverse: 5'AGGGCATTYTGACAAAKCGTCTA 3' [61]. Relative amounts of mRNA expression were normalized to *Rn18s* rRNA.

Subcellular fractionation of mouse embryonic fibroblast

WT control and Δ WD MEFs were cultured until confluent, harvested by scraping and homogenate pelleted at ($14,000 \times g$, 5 min, 4°C). The pellet was homogenized on ice by passing through a 23 G needle and lysed cells pelleted at ($100 \times g$, 10 minutes, 4°C) with post nuclear supernatant (PNS) collected. MEF homogenates were fractionated using a discontinuous step gradient (5–50%) of sucrose (Sigma Aldrich, S0389)-Nycodenz (ProGen 18,003) across a total volume of 1.4 ml. Tubes were loaded into a Beckman TLS-55 ultracentrifugation rotor. Samples were separated by ultracentrifugation at ($61,725 \times g$, 3 hours, 4°C), $7 \times 200 \mu$ l fractions were collected and protein concentration quantified using a bicinchoninic acid (BCA) assay.

Subcellular fractionation of mouse brain

WT and Δ WD mice were sacrificed and brains extracted, weighed, and minced. Tissue was collected and pelleted by centrifugation. The pellet was resuspended in ice cold hypotonic buffer (10 mM Tris-HCl, pH 7.4, 1 mM EDTA), and incubated on ice for 1 minute. Hypotonic buffer was removed through centrifugation before resuspension in 2 ml of buffered sucrose solution and homogenization using a Dounce homogenizer (Kimble 88,502). Lysates were sonicated on ice for 30 s twice before pelleting to remove nuclei, with the PNS fraction collected. Subcellular fractionation of mouse brains was performed on a 32-mL discontinuous (0–30%) Nycodenz gradient in a Beckman SW32 Ti ultracentrifuge rotor. Samples were separated by ultracentrifugation ($59,333 \times g$, 3 hours,

4°C). Afterwards, 8×3.5 ml fractions were collected and stored at -20°C . Protein concentration in PNS and subcellular fractions was quantified using BCA.

Protein expression

MEF plasma membrane fractions were detected using polyclonal ITGB1/ β 1-integrin staining (gift from Uli Mayer, University of East Anglia). Brain plasma membrane fractions were detected with a rabbit anti sodium-potassium ATPase (EP1845Y; abcam 76,020). For plasma membrane isolation, protein bands were quantified by automated densitometry performed using Odyssey CLx software. Densitometry readings were then standardized against fraction protein concentration, determined via BCA, with fractions containing the highest concentration of plasma membrane protein denoted as the plasma membrane peak fractions and assayed for cholesterol concentration.

Biochemical analysis of cholesterol

Cholesterol concentrations were measured using the Amplex® Red cholesterol assay kit (Invitrogen, A12216) according to the manufacturer's instructions. Resorufin fluorescence was measured on a SpectraMax M2 microplate reader (excitation: 545 nm, emission: 590 nm). Cholesterol quantifications were then normalized to protein concentration of the sample as determined by BCA.

Lipid localization

Cholesterol was localized using either D4H mCherry probe or filipin III. D4H mCherry plasmid was kindly provided by Gregory D. Fairn (Dept of Biochemistry, University of Toronto, Toronto, Ontario). Lact-C2-GFP plasmid was purchased from Addgene (22852; deposited by Sergio Grinstein). Plasmids were purified using a NucleoBond® Xtra Midi prep kit (Machery Nagel 12,798,402). Plasmids were transfected into WT and Δ WD MEFs in a 24-well lplate using Lipofectamine 3000 reagent (ThermoFisher, L3000001). Cells were then fixed using 4% PFA for 10 minutes; permeabilized in 0.1% Triton X-100 for 10 minutes; blocked in 0.1 M glycine and 0.5% BSA solutions for 20 and 30 minutes, respectively; and stained with either rabbit anti-RAB7 (late endosomes; Cell Signaling Technology, D95F2), anti-LAMP1 (lysosomes; Cell Signaling Technology, 9091) or anti-EEA1 (early endosomes; Cell Signaling Technology, 2411) at 4°C overnight. Staining with Alexa Fluor® 488 or 594 (abcam, ab150080, ab150077) was performed before mounting and image using either a Zeiss M2 Imager or a Zeiss LSM980-Airyscan confocal microscope. For filipin staining of tissue: tissues were frozen using optimal cutting temperature compound (OCT; Tissue-Tek, 4583) in liquid nitrogen chilled isopentane. Specimens were cut ($10 \mu\text{m}$) and mounted onto a microscope slide, fixed in 4% PFA and stained with 0.5 mg/mL filipin III (Sigma Aldrich, F4767) in PBS + 1% BSA for 2 hours at RT. Lung slices were also stained with anti-RAB7. For filipin staining of MEFs: cells were fixed with 4% PFA and

stained in 0.5 mg/mL filipin III in PBS + 1% BSA for 2 hours at room temperature. Coverslips were mounted and viewed using a Zeiss LSM980-Airyscan confocal microscope with the 405 nm laser.

Statistics

For comparative analysis between two groups, Mann Whitney U tests and independent samples t-tests were carried out where appropriate. For imaging, background staining exclusion and Pearson's correlation coefficients determined using Imaris imaging colocalization software and ImageJ. CellProfiler and Python were used in the acquisition and processing of the endocytosis assay data.

Acknowledgements

We thank Gregory Fairn, Dept of Biochemistry University of Toronto, Toronto, Ontario for the D4H-mcherry plasmid, James McColl (Faculty of Science, UEA) for help with confocal imaging and Naiara Beraza (Quadram Institute) for T0901317 treatment of mice.

Disclosure statement

No potential conflict of interest was reported by the author(s).

Funding

The work was supported by the Biotechnology and Biological Sciences Research Council [BB/M011216/1]; Biotechnology and Biological Sciences Research Council [BB/R00904X/1]; Medical Research Council [MR/R015937/1].

ORCID

Penny P. Powell  <http://orcid.org/0000-0002-5347-0490>

References

- Romanov J, Walczak M, Ibricic I, et al. Mechanism and functions of membrane binding by the Atg5-Atg12/Atg16 complex during autophagosome formation. *Embo J*. 2012;31(22):4304–4317. doi: 10.1038/emboj.2012.278
- Münz C. Non-canonical functions of autophagy proteins in immunity and infection. *Mol Aspects Med*. 2021;82:100987.
- Heckmann BL, Green DR. LC3-associated phagocytosis at a glance. *J Cell Sci*. 2019;132(5):jcs222984.
- Sanjuan MA, Dillon CP, Tait SWG, et al. Toll-like receptor signaling in macrophages links the autophagy pathway to phagocytosis. *Nature*. 2007;450(7173):1253–1257.
- Hamaoui D, Subtil A. ATG16L1 functions in cell homeostasis beyond autophagy. *FEBS J*. 2022;289(7):1779–1800.
- Dooley HC, Razi M, Polson HEJ, Stephen E et al WIP1 links LC3 conjugation with PI3P, autophagosome formation, and pathogen clearance by recruiting Atg12–5–16L1. *Mol Cell*. 2014;55:238–252.
- Strong LM, Chang C, Riley JF, et al. Structural basis for membrane recruitment of ATG16L1 by WIP1 in autophagy. *Elife*. 2021;10. doi: 10.7554/eLife.70372
- Durgan J, Florey O. Many roads lead to CASM: diverse stimuli of noncanonical autophagy share a unifying molecular mechanism. *Sci Adv*. 2022 8;8(43). doi: 10.1126/sciadv.abo1274
- Rai S, Arasteh M, Jefferson M, et al. The ATG5-binding and coiled coil domains of ATG16L1 maintain autophagy and tissue homeostasis in mice independently of the WD domain required for LC3-associated phagocytosis. *Autophagy*. 2019;15:599–612.
- Fletcher K, Ulferts R, Jacquin E, et al. The WD40 domain of ATG16L1 is required for its non-canonical role in lipidation of LC3 at single membranes. *Embo J*. 2018;37(4). doi: 10.15252/emboj.201797840
- Wang Y, Ramos M, Jefferson M, et al. Control of infection by LC3 associated phagocytosis, CASM and detection of raised vacuolar pH by the vAtpase-ATG16L1 axis. *Sci Adv*. 2022 8;8(43). doi: 10.1126/sciadv.abn3298
- Fischer TD, Wang C, Padman BS, et al. STING induces LC3B lipidation onto single-membrane vesicles via the V-ATPase and ATG16L1-WD40 domain. *J Cell Biol*. 2020;219:e202009128.
- Hooper KM, Jacquin E, Li T, et al. V-ATPase is a universal regulator of LC3 associated phagocytosis and non-canonical autophagy. *J Cell Biol*. 2021;221:221 e202105112.
- Xu Y, Zhou P, Cheng S, et al. A bacterial effector reveals the V-ATPase-ATG16L1 axis that initiates xenophagy. *Cell*. 2019;178(3):552–566.e20.
- Ulferts R, Marcassa E, Timimi L, et al. Subtractive CRISPR screen identifies the ATG16L1/vacuolar ATPase axis as required for non-canonical LC3 lipidation. *Cell Rep*. 2021;37(4):109899. doi: 10.1016/j.celrep.2021.109899
- Timimi L, Wrobel AG, Chiduzza GN, et al. The V-ATPase/ATG16L1 axis is controlled by the V1H subunit. *Mol Cell*. 2024;84(15):2966–2983.
- Cadwell K, Liu JY, Brown SL, et al. A key role for autophagy and the autophagy gene Atg16l1 in mouse and human intestinal paneth cells. *Nature*. 2008;456(7219):259–263.
- Wang Y, Sharma P, Jefferson M, et al. Non-canonical autophagy functions of ATG16L1 in epithelial cells limit lethal infection by influenza a virus. *Embo J*. 2021;40(6):e105543.
- Lamprinak D, Beasy G, Zhekova A, et al. LC3-associated phagocytosis is required for dendritic cell inflammatory cytokine response to gut commensal yeast *Saccharomyces cerevisiae*. *Front Immunol*. 2017;8:1397. doi: 10.3389/fimmu.2017.01397
- Serramito-Gómez I, Boada-Romero E, Villamuera R, et al. Regulation of cytokine signaling through direct interaction between cytokine receptors and the ATG16L1 WD40 domain. *Nat Commun*. 2020;11(1):5919. doi: 10.1038/s41467-020-19670-4
- Heckmann BL, Teubner BJW, Boada-Romero E, et al. Noncanonical function of an autophagy protein prevents spontaneous Alzheimer's disease. *Sci Adv*. 2020;6(33):eabb9036.
- Heaton NS, Randall G. Multifaceted roles for lipids in viral infection. *Trends Microbiol*. 2011;19(7):368–375.
- Sieczkarski SB, Whittaker GR. Influenza virus can enter and infect cells in the absence of clathrin-mediated endocytosis. *J Virol*. 2002;76(20):10455–10464. doi: 10.1128/JVI.76.20.10455-10464.2002
- Barman S, Nayak DP. Lipid raft disruption by cholesterol depletion enhances influenza a virus budding from MDCK cells. *J Virol*. 2007;81(22):12169–12178.
- Amini-Bavil-Olyae S, Choi YJ, Lee JH, et al. The antiviral effector IFITM3 disrupts intracellular cholesterol homeostasis to block viral entry. *Cell Host Microbe*. 2013;13(4):452–464. doi: 10.1016/j.chom.2013.03.006
- Tan MJM, Mellouk N, Osborne SE, et al. An ATG16L1-dependent pathway promotes plasma membrane repair and limits listeria monocytogenes cell-to-cell spread. *Nat Microbiol*. 2018;3(12):1472–1485. doi: 10.1038/s41564-018-0293-5
- Tan MJM, Mellouk N, Brumell JH. An autophagy-independent role for ATG16L1: promoting lysosome-mediated plasma membrane repair. *Autophagy*. 2019;15(5):932–933.
- Banerjee I, Yamauchi Y, Helenius A, et al. High-content analysis of sequential events during the early phase of influenza a virus infection. *PLOS ONE*. 2013;8(7):e68450.
- Komal A, Noreen M, El-Kott AF. TLR3 agonists: RGC100, ARNAX, and poly-ic: a comparative review. *Immunol Res*. 2021;69(4):312–322. doi: 10.1007/s12026-021-09203-6

- [30] Askovich PS, Sanders DJ, Rosenberger CM, et al. Differential host response, rather than early viral replication efficiency, correlates with pathogenicity caused by influenza viruses. *PLOS ONE*. 2013;8(9):e74863.
- [31] Yamauchi Y, Helenius A. Virus entry at a glance. *J Cell Sci*. 2013;126(6):1289–1295. doi: [10.1242/jcs.119685](https://doi.org/10.1242/jcs.119685)
- [32] Lu F, Liang Q, Abi-Mosleh L, et al. Identification of NPC1 as the target of U18666A, an inhibitor of lysosomal cholesterol export and ebola infection. *Elife*. 2015;4:e12177.
- [33] Gomes B, Gonçalves S, Disalvo A, et al. Effect of 25-hydroxycholesterol in viral membrane fusion: insights on HIV inhibition. *Biochim et Biophys Acta (BBA) - Biomembr*. 2018;1860(5):1171–1178.
- [34] Wang S, Li W, Hui H, et al. Cholesterol 25-hydroxylase inhibits SARS-CoV-2 and other coronaviruses by depleting membrane cholesterol. *Embo J*. 2020;39(21):e106057.
- [35] Gold ES, Diercks AH, Podolsky I, et al. 25-hydroxycholesterol acts as an amplifier of inflammatory signaling. *Proc Natl Acad Sci U S A*. 2014;111(29):10666–10671.
- [36] Maekawa M. Domain 4 (D4) of perfringolysin O to visualize cholesterol in cellular membranes—the update. *Sensors (Basel)*. 2017;17(3):504. doi: [10.3390/s17030504](https://doi.org/10.3390/s17030504)
- [37] Maekawa M, Fairn GD. Complementary probes reveal that phosphatidylserine is required for the proper transbilayer distribution of cholesterol. *J Cell Sci*. 2015;128(7):1422–1433. doi: [10.1242/jcs.164715](https://doi.org/10.1242/jcs.164715)
- [38] Fairn GD, Schieber NL, Ariotti N, et al. High-resolution mapping reveals topologically distinct cellular pools of phosphatidylserine. *J Cell Biol*. 2011;194(2):257–275.
- [39] Zanotti I, Poti F, Pedrelli M, et al. The LXR agonist T0901317 promotes the reverse cholesterol transport from macrophages by increasing plasma efflux potential. *J Lipid Res*. 2008;49(5):954–960. doi: [10.1194/jlr.M700254-JLR200](https://doi.org/10.1194/jlr.M700254-JLR200)
- [40] Winkler MBL, Kidmose RT, Szomek M, et al. Structural insight into eukaryotic sterol transport through niemann-pick type C proteins. *Cell*. 2019;179(2):485–497.e18. doi: [10.1016/j.cell.2019.08.038](https://doi.org/10.1016/j.cell.2019.08.038)
- [41] Qian H, Wu X, Du X, et al. Structural basis of low-pH-dependent lysosomal cholesterol egress by NPC1 and NPC2. *Cell*. 2020;182(1):98–111.e18.
- [42] Castellano BM, Thelen AM, Moldavski O, et al. Lysosomal cholesterol activates mTORC1 via an SLC38A9–niemann-Pick C1 signaling complex. *Science*. 2017;355(6331):1306–1311. doi: [10.1126/science.aag1417](https://doi.org/10.1126/science.aag1417)
- [43] Nakatsu F, Kawasaki A. Functions of oxysterol-binding proteins at membrane contact sites and their control by phosphoinositide metabolism. *Front Cell Dev Biol*. 2021;9:Article 664788.
- [44] Huynh KK, Gershenson E, Grinstein S. Cholesterol accumulation by macrophages impairs phagosome maturation. *J Bio Chem*. 2008;283(51):35745–35755. doi: [10.1074/jbc.M80623200](https://doi.org/10.1074/jbc.M80623200)
- [45] Noda NN. Atg2 and Atg9: intermembrane and interleaflet lipid transporters driving autophagy. *Biochim et Biophys Acta (BBA) - Mol Cell Biol Lipids*. 2021;1866(8):158956.
- [46] Liao Z, Cimaskasy LM, Hampton R, et al. Lipid rafts and HIV pathogenesis: host membrane cholesterol is required for infection by HIV type 1. *AIDS Res Hum Retroviruses*. 2001;17(11):1009–1019. doi: [10.1089/088922201300343690](https://doi.org/10.1089/088922201300343690)
- [47] Graham DR, Chertova E, Hilburn JM, et al. Cholesterol depletion of human immunodeficiency virus type 1 and simian immunodeficiency virus with beta-cyclodextrin inactivates and permeabilizes the virions: evidence for virion-associated lipid rafts. *J Virol*. 2003;77(15):8237–8248.
- [48] Sun X, Whittaker GR. Role for influenza virus envelope cholesterol in virus entry and infection. *J Virol*. 2003;77(23):12543–12551.
- [49] Martin PK, Marchiando A, Xu R, et al. Autophagy proteins suppress protective type I interferon signalling in response to the murine gut microbiota. *Nat Microbiol*. 2018;3(10):1131–1141. doi: [10.1038/s41564-018-0229-0](https://doi.org/10.1038/s41564-018-0229-0)
- [50] Chu H, Khosravi A, Kusumawardhani IP, et al. Gene-microbiota interactions contribute to the pathogenesis of inflammatory bowel disease. *Science*. 2016;352(6289):1116–1120.
- [51] Schreurs RRCE, Koulis A, Booiiman T, et al. Autophagy-enhancing ATG16L1 polymorphism is associated with improved clinical outcome and T-cell immunity in chronic HIV-1 infection. *Nat Commun*. 2024;15(1):2465.
- [52] Lassen KG, Kuballa P, Conway KL, et al. Atg16L1 T300A variant decreases selective autophagy resulting in altered cytokine signaling and decreased antibacterial defense. *Proc Natl Acad Sci USA*. 2014;111(21):7741–7746.
- [53] Cao X. ISG15 secretion exacerbates inflammation in SARS-CoV-2 infection. *Nat Immunol*. 2021;22(11):1360–1362.
- [54] Vercammen E, Staal J, Beyaert R. Sensing of viral infection and activation of innate immunity by toll-like receptor 3. *Clin Microbiol Rev*. 2008;21(1):13–25. doi: [10.1128/CMR.00022-07](https://doi.org/10.1128/CMR.00022-07)
- [55] Coch C, Stümpel JP, Lilien-Waldau V, et al. RIG-I activation protects and rescues from lethal influenza virus infection and bacterial superinfection. *Mol Ther*. 2017;25(9):2093–2103. doi: [10.1016/j.ymthe.2017.07.003](https://doi.org/10.1016/j.ymthe.2017.07.003)
- [56] Brauer R, Chen P. Influenza virus propagation in embryonated chicken eggs. *J Vis Exp*. 2015;(97):52421.
- [57] Gammoh N. The multifaceted functions of ATG16L1 in autophagy and related processes. *J Cell Sci*. 2020;133(20). doi: [10.1242/jcs.249227](https://doi.org/10.1242/jcs.249227)
- [58] Gauth CR, Smith TF. Replication and plaque assay of influenza virus in an established line of canine kidney cells. *Appl Microbiol*. 1968;16(4):588–594. doi: [10.1128/am.16.4.588-594.1968](https://doi.org/10.1128/am.16.4.588-594.1968)
- [59] Liu R, An L, Liu G, et al. Mouse lung slices: an ex vivo model for the evaluation of antiviral and anti-inflammatory agents against influenza viruses. *Antiviral Res*. 2015;120:101–111. doi: [10.1016/j.antiviral.2015.05.008](https://doi.org/10.1016/j.antiviral.2015.05.008)
- [60] Stauffer S, Feng Y, Nebioglu F, et al. Stepwise priming by acidic pH and a high K⁺ concentration is required for efficient uncoating of influenza A virus cores after penetration. *J Virol*. 2014;88(22):13029–13046. doi: [10.1128/JVI.01430-14](https://doi.org/10.1128/JVI.01430-14)
- [61] WHO information for the molecular detection of influenza viruses. 2021. Available from: https://cdn.who.int/media/docs/default-source/influenza/molecular-detection-of-influenza-viruses/protocols_influenza_virus_detection_feb_2021.pdf